Environmental Science & Technology

pubs.acs.org/est

Open Access

This article is licensed under CC-BY-NC-ND 4.0

Article

A Diffusion-Driven CH_4–O_2 Boundary Structures Methane Oxidation and Carbon Transformation in Upland Soils

Alexander B. Chase,* J.R.R. Navodi Jayarathne, Motahare Haghighatjoo, Neil J. Tabor, and Kathleen M. Smits

Cite This: *Environ. Sci. Technol.* 2026, 60, 22397–22407

Read Online

ACCESS | Metrics & More | Article Recommendations | Supporting Information

ABSTRACT: Although extensive work has characterized high-affinity atmospheric methane oxidation in upland soils and sustained oxidation in chronically methane-rich environments, shallow point-source inputs introduce transient methane pulses into otherwise aerated heterotrophic soils. Whether these pulses migrate rapidly toward the atmosphere or instead create localized redox boundaries that restructure soil carbon pools and microbial metabolism remains unclear. Here, we conducted a controlled natural gas release experiment to quantify coupled geochemical and microbial responses in near-surface soils across a methane gradient. The release produced a spatial interval where measured CH_4 and reconstructed O_2 availability overlapped, identifying a redox transition associated with shifts in carbon geochemistry and methane-oxidation-related functional potential. Spatially resolved $\delta^{13}C$ and C:N measurements revealed strong ^{13}C enrichment of soil organic carbon (SOC) at the plume center, while elevated carbonate abundance and isotope composition distinguished a geochemical transition between the methane-rich plume center and distal reference soils. Within the intermediate CH_4–O_2 overlap zone, methane-associated monooxygenases (MMOs) and C_1 assimilation genes were coordinately enriched, supporting structured C_1 metabolic potential across the redox boundary. Metagenomic assembly and reconstruction linked this methane-responsive interval to Actinomycetota-affiliated genomes encoding expanded monooxygenase repertoires, including sMMO-like systems supported by operon architecture and catalytic-subunit phylogeny. This association provides a mechanistic link between transient methane exposure, redox-boundary formation, and microbial carbon transformation in aerated soils. Together, these findings show that shallow methane inputs can generate spatially constrained biogeochemical hotspots where gas transport, carbonate accumulation, and monooxygenase-associated C_1 assimilation converge, and define conditions under which soil processes may influence methane transport toward the atmosphere.

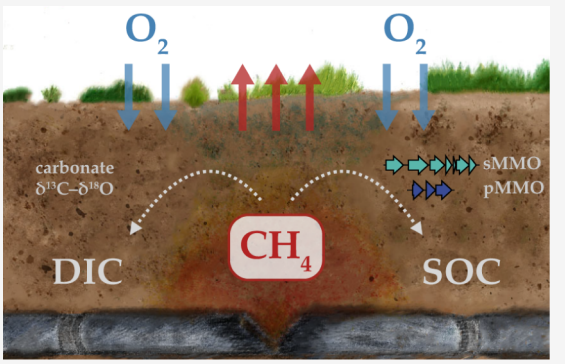

KEYWORDS: *soil biogeochemistry, methane oxidation, microbial carbon cycling, isotopic signatures, facultative methanotrophs*

INTRODUCTION

Methane (CH_4) is a potent greenhouse gas and a central component of the global carbon cycle.[1] In terrestrial systems, soils function as both sources and sinks of methane, depending on the balance between production, transport, and microbial oxidation.[2,3] Upland soils, defined here as relatively aerated, unsaturated soils that are not persistently inundated or methanogenic, represent a globally significant sink for atmospheric methane and account for a substantial fraction of biological CH_4 consumption.[4,5] Aerobic methane-oxidizing microorganisms mediate this sink and form the dominant biological control on atmospheric methane uptake.[2,6] Methane oxidation in upland soils is not uniformly distributed but instead occurs along redox interfaces structured by gas diffusion, oxygen availability, soil moisture, and physical heterogeneity.[7,8] These interfaces are especially important during shallow subsurface methane leakage, where upward methane transport intersects O_2 supplied by atmospheric diffusion and near-surface gas exchange. Because the depth, thickness, and lateral position of this overlap zone can shift across fine spatial and temporal scales, process-based models that rely on simplified reaction parametrizations or extrapolate from a narrow set of model organisms[9,10] remain limited in their ability to predict how methane oxidation responds to transient methane inputs and evolving redox structure.[11−13]

Mechanistic understanding of soil methanotrophy derives largely from two contrasting settings: high-affinity atmospheric methane oxidation in upland soils[14,15] and sustained methane oxidation in chronically methane-enriched environments such

Received: March 6, 2026
Revised: July 28, 2026
Accepted: July 29, 2026
Published: August 7, 2026

ACS Publications

© 2026 The Authors. Published by American Chemical Society

Downloaded from pubs.acs.org/esthag/article-pdf/60/32/22397/6456396/acs.est.6c03515.pdf by guest on 19 August 2026

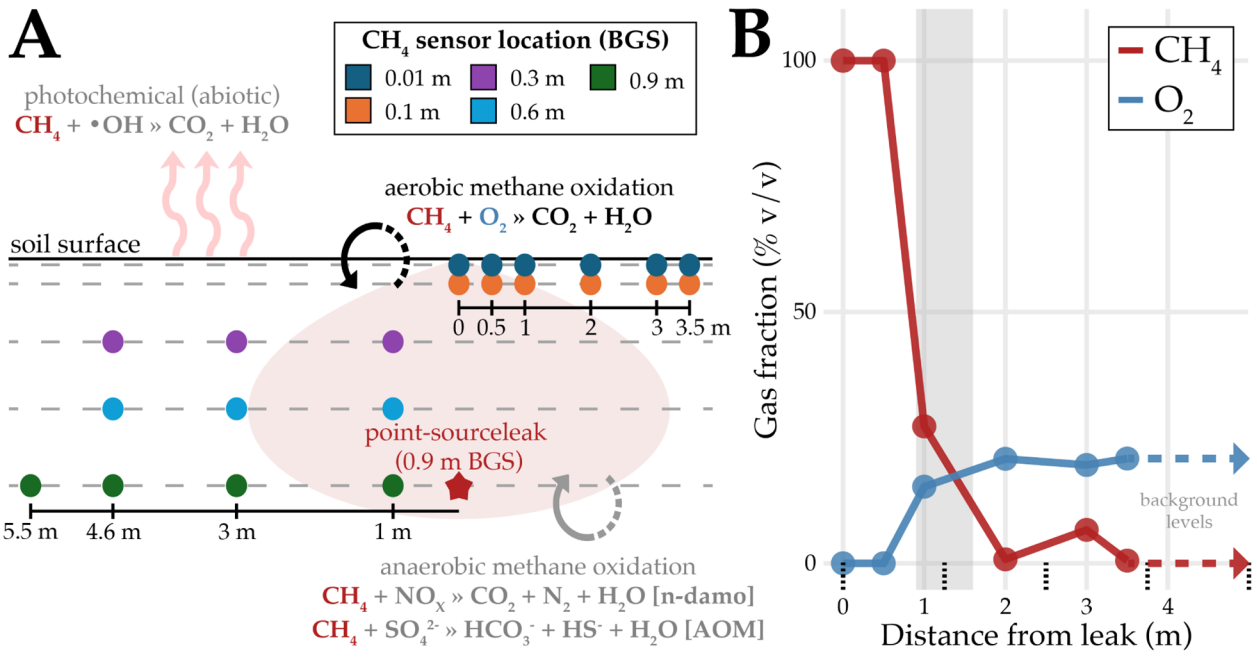

Figure 1. Spatial structure of the near-surface methane plume. A) Conceptual schematic (not to scale) of the controlled-release showing the subsurface methane plume, near-surface transition zone, and gas-sensor positions; detailed testbed geometry is shown in Figure S1. B) Gas-phase CH_4 and reconstructed O_2 availability at 0.01 m below the ground surface (BGS) on release day 2. Points show discrete gas-sensor measurements for CH_4 and modeled estimates for O_2. Dotted vertical lines indicate soil-sampling radii; soil samples were collected from nearby noninstrumented locations to avoid disturbing sensors and release infrastructure. The shaded region denotes the inferred transition zone, not a directly measured boundary. CH_4 declined toward background levels at distal sample locations (see Figures S2 and S3).

as wetlands,[16] rice paddies,[17] and permafrost soils.[18] These systems have provided foundational insights into methane oxidation kinetics and physiology,[19] but they do not fully capture the diffusion-limited and spatially transient conditions generated by shallow subsurface methane inputs. Under these conditions, methane enters heterotrophic soils as both a reduced carbon input and a redox perturbation that interacts with established soil organic carbon (SOC) pools. Methane pulses may therefore have contrasting effects across fine spatial gradients: gas-saturated zones can restrict pore-gas exchange and impose physiological stress, while suitable redox conditions support methane-derived C_1 metabolism.[20−22] Such transient interfaces may favor metabolically flexible or facultative lineages within heterotrophic soils, including members of Actinomycetota and Verrucomicrobiota, whose contributions to methane and short-chain hydrocarbon oxidation remain incompletely resolved.[23−26] As a result, the extent to which shallow CH_4−O_2 boundaries are associated with methane oxidation potential, downstream C_1 assimilation, and SOC restructuring in upland soils remains poorly constrained.

This limitation is particularly important for anthropogenic leakage from natural gas infrastructure, compromised wells, and abandoned wells, which substantially contribute diffuse methane emissions to regional budgets.[27] In these systems, soil-mediated oxidation may attenuate emissions before methane reaches the atmosphere; for example, microbial CH_4 oxidation produces CO_2 that can enter dissolved inorganic carbon (DIC) pools and interact with abiotic carbonate chemistry.[28,29] The same redox structure that constrains oxidation can therefore alter alkalinity and carbonate precipitation, with consequences for SOC composition and isotopic signatures.[30−32] Resolving these interconnected physical, chemical, and biological processes requires controlled field experiments that preserve realistic soil structure, gas dynamics, atmospheric exchange, and resident microbial communities while allowing methane source conditions to be constrained.[33−35] More broadly, understanding how microbial metabolism responds to these transient gradients is critical for predicting the extent to which aerated soils attenuate episodic methane emissions across both anthropogenic leakage systems and natural transient methane inputs.

Here, we conducted a controlled natural gas release experiment to quantify soil geochemical and microbial responses to shallow methane input under field-relevant leak conditions, with particular focus on the near-surface interval where methane supply and oxygen availability overlap. By integrating pore-gas reconstruction, stable isotope analyses, carbonate measurements, and metagenomic profiling, we tested how a spatially restricted CH_4−O_2 boundary structures methane oxidation potential and downstream C_1 assimilation pathways *in situ*. We predicted that this overlap zone would show coordinated enrichment of monooxygenase genes and C_1 assimilation modules, accompanied by geochemical patterns consistent with methane-associated carbon transformation. By linking subsurface gas dynamics, solid-phase carbon-pool restructuring, and microbial functional potential, this study provides spatially resolved observations of how methane-attenuation potential is organized across fine-scale redox and gas-transport gradients.

RESULTS

Methane Concentration Dynamics during Controlled Leak

We characterized subsurface and near-surface methane concentration dynamics during a seven-day monitoring period

Downloaded from pubs.acs.org/esthag/article-pdf/60/32/22397/6456396/acs.est.6c03515.pdf by guest on 19 August 2026

https://doi.org/10.1021/acs.est.6c03515
Environ. Sci. Technol. 2026, 60, 22397−22407

at the Methane Emissions Technology Evaluation Center (METEC), including a five-day controlled natural gas release and two days of postrelease monitoring (Figure 1A; Figure S1). Methane injected 0.9 m below ground surface (BGS) generated a vertically coherent plume centered above the release point. Within approximately 6 h of release initiation, CH_4 concentrations at 0.3−0.9 m BGS stabilized near saturation (≈100% CH_4 v/v; v/v = volume per volume of gas-filled pore space) within 1 m of the emission source, exhibiting minimal vertical stratification under quasi-steady conditions (Figure S2). At greater radial distances, concentrations declined and vertical gradients became increasingly pronounced, reflecting lateral dilution and depth-dependent transport through the soil matrix.

Near-surface measurements during the release captured rapid upward propagation of methane together with the spatially confined lateral extent of the surface plume. Methane from the subsurface release was first detected above ambient levels at the surface within 10 min, then expanded outward over the next 24 h: reaching 1 m within 30 min, 3 m within 5 h, and 4.5 m within 16 h (Figure S2). By day 2, surface mapping showed that the plume remained highly localized: CH_4 concentrations reached ≈38% v/v directly above the leak, but decreased sharply with distance, with a 23-fold reduction at 0.5 m (1.6% v/v) and 40-fold at 1 m (0.9% v/v). Beyond 3.5 m, surface soil CH_4 concentrations fell below detector threshold (<0.1% v/v; Figure S3). Concurrent METEC monitoring during the experimental period measured background atmospheric CH_4 concentrations of 1.95−2.3 ppm, more than 4 orders of magnitude lower than peak surface plume concentrations observed directly above the leak. Soil temperature and moisture remained stable throughout the release (Figure S4), indicating that plume structure was governed primarily by gas transport rather than short-term hydrologic or thermal variability.

Vertical gas exchange in shallow soils is also influenced by atmospheric pressure fluctuations and soil hydraulic properties; therefore, we integrated methane time series with colocated soil moisture profiles to estimate gas-filled porosity and reconstruct near-surface O_2 availability. Directly above the leak, elevated methane was inferred to displace atmospheric gases, producing near-complete O_2 limitation under the model assumptions (Figure S5). At intermediate distances, methane remained elevated while O_2 availability persisted. These combined gradients supported an inferred near-surface interval (approximately 1.0−1.5 m from the leak) where elevated CH_4 coincided with inferred O_2 availability on day 2 (Figure 1B). Distances <1 m were characterized by CH_4 saturation and O_2 limitation, whereas >1.5 m methane concentrations declined toward distal reference levels. Together, these observations delineate the spatial structure of the plume and define the near-surface interval where elevated methane coincided with oxygen availability consistent with aerobic methane oxidation potential.

Soil Biogeochemistry and Isotopic Signatures across the Methane Gradient

To evaluate how organic and inorganic carbon pools varied across the methane gradient, we analyzed surface soils collected on day 2 of the release across five radial distances from the emission point (N = 34). Day 2 sampling coincided with a quasi-steady methane plume and inferred near-surface CH_4−O_2 transition zone (Figure 1B), providing a single time-point spatial assessment of soil geochemical conditions across the methane gradient. Acid-rinsed and untreated aliquots yielded broadly similar spatial patterns in $\delta^{13}C$ and C:N values (Figure S6; Table S1). Acid treatment resulted in a small but significant ^{13}C shift (Figure S7A; mean difference = 0.84 ± 2.00‰, $p < 0.05$), consistent with minor removal of ^{13}C-enriched carbonate. However, radial trends in $\delta^{13}C$ were preserved regardless of treatment (untreated slope = −0.63‰ m^{-1}; rinsed slope = −1.18‰ m^{-1}), indicating that carbonate removal did not alter underlying spatial patterns (Figure S7B).

Acid rinsing reduced carbonate influence on the organic fraction and revealed a strong plume-center isotopic and stoichiometric signal. Soils collected directly above the emission source (0 m) exhibited strong ^{13}C enrichment relative to all other distances ($mean_{0m}$ = −13.1 ± 0.8 vs $mean_{1.25-5m}$ = −24.7 ± 2.0; Welch's t test, $p < 0.01$). C:N ratios were also elevated at 0 m ($mean_{0m}$ = 15.2 ± 0.4 vs $mean_{1.25-5m}$ = 10.9 ± 1.8; Welch's t test, $p < 0.001$), indicating that plume-center ^{13}C enrichment was accompanied by a localized shift in organic matter stoichiometry (Figure 2).

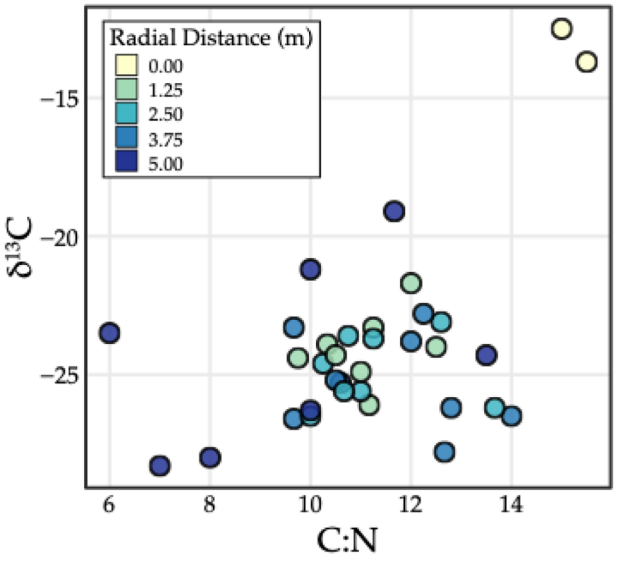

Figure 2. Soil isotopic and stoichiometric patterns across the methane gradient. Acid-rinsed organic $\delta^{13}C$ values plotted against C:N ratios for surface soils collected from the METEC experimental site. Points are colored by radial distance from the emission source.

Beyond the plume center, samples from nonzero distances occupied a broader overlapping region of $\delta^{13}C$−C:N space, indicating that the acid-rinsed organic fraction captured a strong plume-center carbon signal but did not resolve a monotonic distance response across the surrounding transect.

In contrast to the organic fraction, independent carbonate isotope compositions identified a transitional geochemical regime at intermediate distances (Figure S8A; Table S2). Carbonate concentrations were highest at 0 m ($mean_{0m}$ = 13.5 ± 4.9%) and declined rapidly with distance, while carbonate isotope values exhibited strong distance-dependent shifts. For example, carbonate $\delta^{13}C$ values converged near −4.5‰ in high-carbonate soils and extended to −38.0‰ at low carbonate concentrations (Figure S8C), consistent with isotope-space mixing between a methane-influenced carbonate endmember proximal to the leak and a lower-carbonate distal reference endmember. Notably, carbonate $\delta^{13}C$ and $\delta^{18}O$

Downloaded from pubs.acs.org/esthag/article-pdf/60/32/22397/6456396/acs.est.6c03515.pdf by guest on 19 August 2026

https://doi.org/10.1021/acs.est.6c03515
Environ. Sci. Technol. 2026, 60, 22397−22407

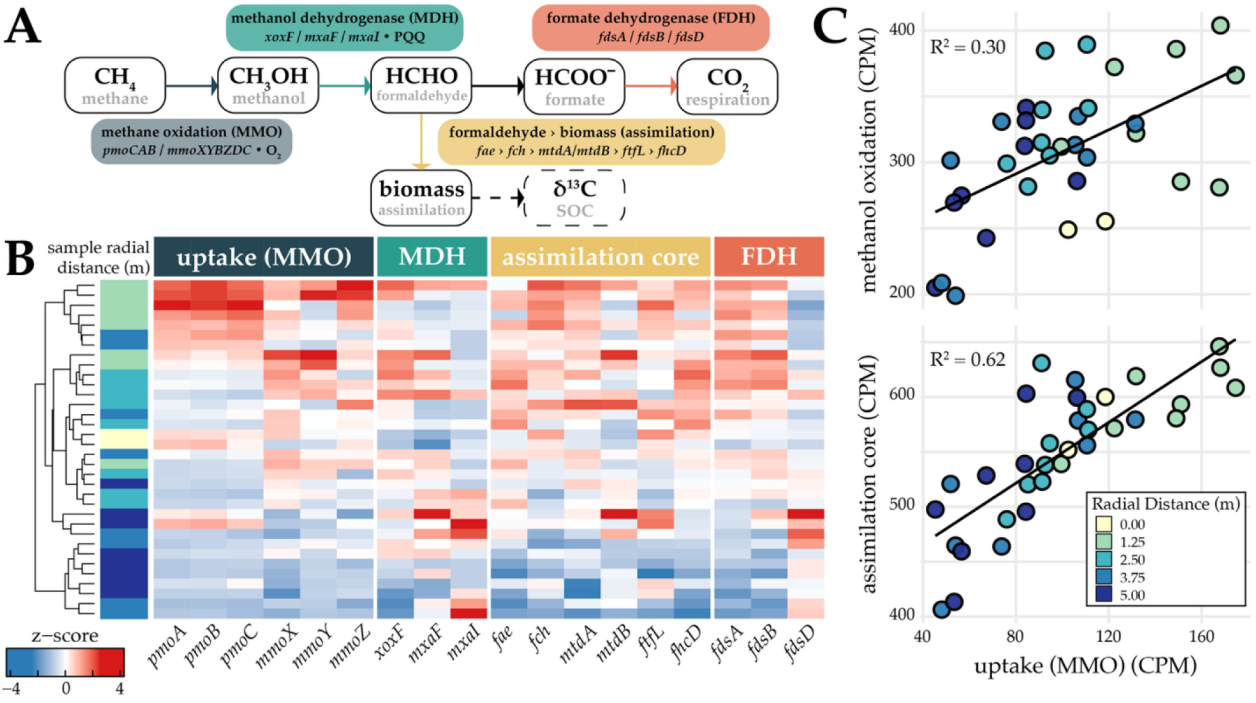

Figure 3. Spatial organization of methane oxidation and C_1 metabolic pathways. A) Schematic representation of surveyed C_1 metabolic pathways. B) Hierarchical clustering of C_1 marker genes across samples (CPM = counts per million PFAM hits; values are normalized as z-scores). Methane monooxygenase (MMO) uptake genes and formaldehyde assimilation genes cluster with samples at intermediate distances (1.25 m). C) Relationships between MMO abundance and downstream C_1 pathways. Positive correlations with methanol oxidation and the formaldehyde assimilation core indicate coordinated C_1 carbon routing across the methane gradient.

values followed a strong isotope-space relationship (R^2 = 0.84; Figure S8B), with samples collected at 1.25 m forming a coherent cluster between carbonate endmembers. Together, the organic-fraction and carbonate-specific isotope data support a two-component mixing system between a CH_4-rich, O_2-limited plume center and distal reference soils, with an intermediate geochemical transition zone.

Microbial Community Composition and Functional Responses across Leak Gradients

We next examined whether microbial community structure and functional potential paralleled the geochemical gradients observed across the day 2 methane plume. Neither overall taxonomic composition nor broad protein-family profiles differed significantly with distance from the leak center (Bray–Curtis; PERMANOVA, taxonomic: R^2 = 0.26, p = 0.20; functional: R^2 = 0.32, p = 0.11; Figure S9A/C). However, functional dispersion differed significantly across distances, with samples at 1.25 m exhibiting reduced within-group variability and separating from distal 5 m soils in ordination space (PERMDISP, $p < 0.01$). Taxonomic dispersion showed a similar but marginal distance effect (p = 0.09). Alpha diversity likewise showed a localized reduction at 1.25 m rather than a broad monotonic distance response; Shannon and Simpson diversity were both reduced at 1.25 m relative to the other sampled distances (planned contrasts, both $p < 0.05$; Figure S9B). Thus, broad taxonomic and functional profiles provided little evidence for whole-community turnover across the methane gradient, but community variability was reduced within the CH_4–O_2 overlap zone.

At the pathway level, methane oxidation showed the strongest distance-associated response among broad protein-family categories (linear models, $p < 0.01$; FDR-adjusted = 0.07; Figure S10A). Relative to distal 5 m soils, where surface CH_4 was below detector threshold (<0.1% v/v; Figure S3), methane oxidation annotations were significantly more abundant at 1.25 and 2.5 m (quasibinomial GLMs; Figure S10A/B), indicating localized enrichment near the CH_4–O_2 overlap zone. In contrast, glycoside hydrolases and carbohydrate-binding modules showed no spatial signal (all FDR > 0.07), indicating that methane-oxidation enrichment was not accompanied by a generalized increase in complex organic carbon degradation capacity.

To further resolve pathway-level structure within C_1 metabolism, we quantified translated, unassembled reads associated with the two major methane monooxygenase systems, including homologues of the membrane-bound particulate methane monooxygenase (pMMO; catalytic subunit *pmoA*) and soluble methane monooxygenase (sMMO; catalytic subunit *mmoX*), along with downstream C_1 genes (Figure 3A). Given the limited resolution of short-read searches among closely related monooxygenase families, including soluble di-iron monooxygenases (SDIMOs) and ammonia monooxygenases (AMO; catalytic subunit *amoA*), we conservatively interpreted these marker sets as *mmoX*/SDIMO and *pmoA*/*amoA* homologues. Both marker sets declined significantly with increasing distance from the source and reached their highest abundances at 1.25 m (Figure S11A; *mmoX*/SDIMO: Kruskal–Wallis $p < 0.01$; Spearman $\rho = -0.63$, $p < 0.001$; *pmoA*/*amoA*: $p < 0.05$; Spearman $\rho = -0.50$, $p < 0.01$). Taxonomic assignments indicated that >90% of classified *mmoX*/SDIMO homologues were Actinomycetota across distances. Assignments of *pmoA*/*amoA* homologue assignments were more heterogeneous, with Actinomycetota

https://doi.org/10.1021/acs.est.6c03515
Environ. Sci. Technol. 2026, 60, 22397–22407

Downloaded from pubs.acs.org/esthag/article-pdf/60/32/22397/6456396/acs.est.6c03515.pdf by guest on 19 August 2026

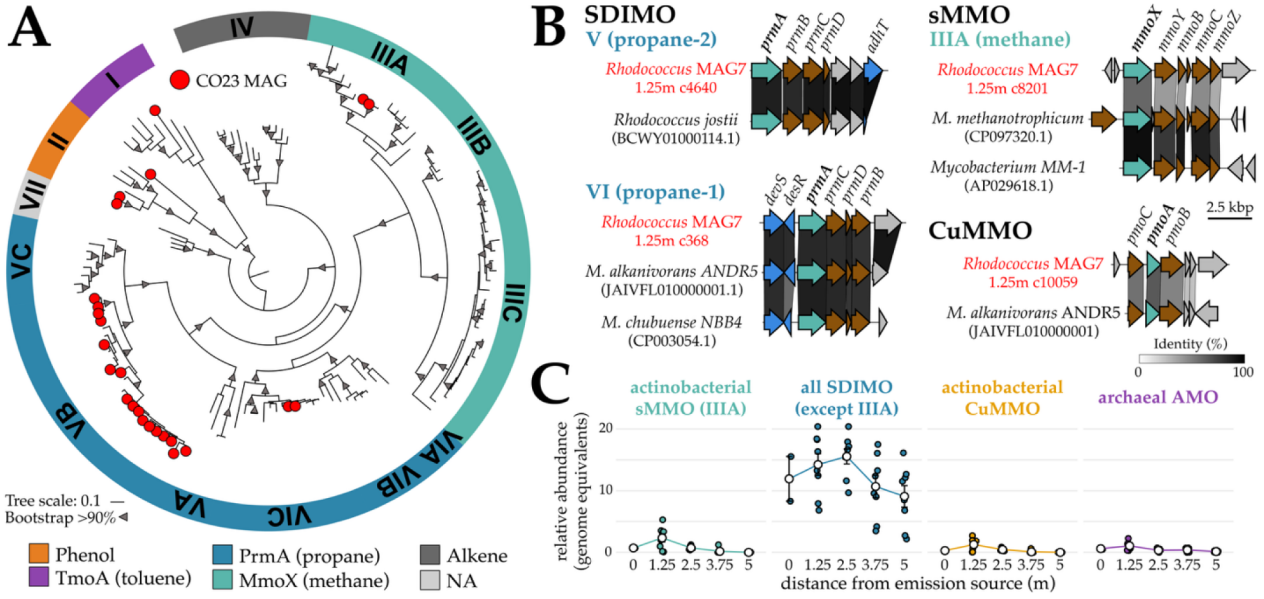

Figure 4. Genome-resolved and phylogenetic characterization of monooxygenase operons across the methane gradient. A) Maximum-likelihood phylogeny of soluble di-iron monooxygenase (SDIMO) catalytic subunits, including *mmoX* and related homologues. Sequences derived from metagenome-assembled genomes (CO23 MAGs) are indicated by red circles. Major SDIMO clades are labeled according to established classifications.[38,52] B) Operon architecture of a high-quality Actinomycetota MAG (*Rhodococcus* MAG_7) recovered from the 1.25 m coassembly and encoding four distinct monooxygenase operons: one copper-containing membrane monooxygenase (CuMMO), two proane monooxygenase-associated SDIMOs, and one type IIIA sMMO-like operon. Representative actinobacterial methane- and alkane-oxidizing reference genomes are shown for comparison. C) Normalized abundance (genome equivalents, CGE) of contigs encoding sMMO-like operons, CuMMO operons, nonmethane SDIMOs, and ammonia monooxygenase (AMO) across soils sampled at increasing radial distance from the methane source. Points represent individual samples; white-centered circles denote means ± standard error.

enriched at 1.25−2.5 m and Pseudomonadota dominating at 5 m (Figure S11B).

Hierarchical clustering of normalized C_1 marker genes revealed coordinated spatial structuring across metabolic modules (Figure 3B). Methane monooxygenase and formaldehyde assimilation genes were enriched near the leak and declined with distance (Figure S12A; $\rho = -0.69$, $p < 0.001$; $\rho = -0.53$, $p < 0.01$, respectively), whereas methanol dehydrogenase and formate dehydrogenase showed no significant distance dependence ($\rho = -0.02$, $p > 0.1$; $\rho = -0.31$, p = 0.07). At the same time, methane monooxygenase abundance positively correlated with both formaldehyde assimilation potential (Figure 3C; $\rho = 0.80$, $p < 0.001$; adjusted $R^2 = 0.62$) and methanol oxidation genes ($\rho = 0.51$, $p < 0.01$; adjusted $R^2 = 0.30$), indicating coordinated enrichment of methane uptake and downstream C_1-processing capacity.

Although classified *mmoX*/SDIMO homologues were strongly affiliated with Actinomycetota (Figure S11B), the broader C_1 functional pattern was not explained by an overall increase in Actinomycetota relative abundance. Specifically, total Actinomycetota abundance did not covary with either methane monooxygenase or formaldehyde assimilation abundance ($\rho = 0.23$ and 0.21, respectively; both $p > 0.1$). Instead, the methane-responsive signal reflected finer-scale variation in monooxygenase-associated functional potential rather than a phylum-wide abundance shift. This variation extended to downstream C_1 metabolism: the assimilation-to-terminal-oxidation index increased significantly with methane monooxygenase abundance ($p < 0.01$; adj. $R^2 = 0.20$; Figure S12B), indicating greater assimilation capacity relative to terminal oxidation at higher methane uptake potential. Together, these patterns suggest that C_1 metabolic potential was spatially structured across the day 2 methane gradient, with coordinated enrichment of uptake and assimilation modules proximal to the leak.

Recovery and Spatial Distribution of Methane Monooxygenase Operons

To recover organisms encoding methane and related hydrocarbon monooxygenases across the methane gradient, we performed distance-specific coassemblies, yielding 1514 genome bins, including 30 high-quality and 80 medium-quality metagenome-assembled genomes (MAGs). All MAG-associated contigs were screened for monooxygenase operons requiring at least three colocalized genes, including the catalytic subunit *mmoX* for sMMO-like operons or *pmoA/amoA* for copper-containing membrane monooxygenase-like (CuMMO-like) operons. After dereplication, we identified 25 nonredundant sMMO-like operons and three CuMMO-like operons.

Phylogenetic and conserved-residue analyses showed that the recovered membrane-bound monooxygenases encoded copper-binding residues characteristic of CuMMOs;[36] however, they likely do not represent canonical particulate methane monooxygenases (pMMOs). The two actinobacterial CuMMOs, recovered from the 1.25 and 2.5 m coassemblies, were phylogenetically affiliated with broader C_2−C_4 hydrocarbon monooxygenases; the Nitrososphaeraceae archaeal CuMMO recovered from the 1.25 m coassembly was classified as an ammonia monooxygenase (AMO) (Figure S13A/B). All recovered CuMMO sequences retained residues corresponding to the Cu_B and Cu_C copper-binding sites, including the Cu_C site implicated in catalytic methane/hydrocarbon oxidation.[37] For example, protein modeling of the *Rhodococcus* MAG_7 CuMMO positioned the predicted Cu_B and Cu_C residues at

https://doi.org/10.1021/acs.est.6c03515
Environ. Sci. Technol. 2026, 60, 22397−22407

Downloaded from pubs.acs.org/esthag/article-pdf/60/32/22397/6456396/acs.est.6c03515.pdf by guest on 19 August 2026

the expected locations within the corresponding subunits of characterized CuMMO complexes (Figure S13C).

The 25 sMMO-like operons were predominantly affiliated with Actinomycetota and distributed across multiple medium- and high-quality MAGs, including distinct *Mycobacterium* MAGs and representatives classified as *Rhodococcus*, *Jatrophihabitans*, and *Pseudocardia* (Figure S14). Putative sMMO-like operons were further classified based on phylogenetic placement of the *mmoX* catalytic subunit within established soluble di-iron monooxygenase (SDIMO) clades[38] (Figure 4A; Figure S14A). This reference-guided classification distinguished type III sMMO-like operons from broader alkane monooxygenase-associated SDIMOs and was supported by operon-architecture comparisons with characterized reference systems (Figure 4B; Figure S14B). Most sequences clustered within group VB, an actinobacterial propane-2-monooxygenase clade; however, two closely related operons from Actinomycetota-affiliated MAGs clustered within the type IIIA sMMO clade associated with recently described actinobacterial methane-oxidizing lineages.[39−41]

To place these operons within broader genomic context, we reconstructed metabolic models for the 35 nonredundant medium- and high-quality MAGs retained after genome dereplication (Figure S15). A high-quality *Rhodococcus* MAG_7 (99.7% completeness, 1.42% contamination), recovered from the 1.25 m coassembly, encoded four distinct monooxygenase operons: one CuMMO affiliated with hydrocarbon monooxygenases (Figure S13C) and three SDIMO operons, including one type IIIA sMMO-like operon and two proane monooxygenases assigned to groups VB and VIC (Figure 4B). The propane-associated operons additionally contained auxiliary functions that may couple hydrocarbon oxidation to oxygen availability, including an alcohol dehydrogenase (*adhT*) within the propane-2 operon and the two-component oxygen-sensing regulatory system (*devS*/*desR*) within the propane-1 operon. These features indicate metabolic and regulatory capacity under fluctuating CH_4−O_2 conditions.

Consistent with this expanded oxidative repertoire, *Rhodococcus* MAG_7 also encoded downstream C_1-processing pathways, including enzymes associated with formaldehyde oxidation and H4F-linked C_1 metabolism (Figure S15). This genome was also the only MAG to encode ribulose monophosphate (RuMP) core markers associated with C_1 assimilation, defined here by the presence of both RuMP core markers *hxlA*/*hxlB* or *hps*/*phi*. Together, these features indicate genomic potential to couple hydrocarbon oxidation with downstream C_1 processing and carbon assimilation. In contrast, other SDIMO-containing MAGs lacked RuMP core markers, with the exception of a single *Mycobacterium* MAG encoding *hxlB* but not *hxlA*, indicative of an incomplete RuMP pathway. Across the MAG set, the co-occurrence of multiple monooxygenase systems and accessory metabolic and regulatory pathways within Actinomycetota genomes indicates expanded oxidative repertoires among lineages recovered at intermediate distances from the leak.

To determine whether these genome-encoded oxidative repertoires were spatially aligned with the methane gradient, we quantified coverage-based abundance of monooxygenase operons across the transect. Both CuMMO- and sMMO-like contigs declined significantly with increasing distance from the leak (Spearman's $\rho = -0.81$ and -0.83, respectively; both $p < 0.001$), with highest abundance at 1.25 m and approaching distal reference levels at 3.75−5 m (Figure 4C). Archaeal ammonia monooxygenases exhibited a similar distance relationship ($\rho = -0.60$, $p < 0.001$), whereas SDIMO contigs outside methane-associated clades showed weaker spatial patterns ($\rho = -0.38$, $p < 0.05$). These assembly based patterns mirror the enrichment of methane monooxygenase genes in unassembled C_1 profiles and align with the inferred CH_4−O_2 overlap zone identified from pore-gas reconstruction (Figure 1B).

DISCUSSION

The spatial coupling of methane availability, solid-phase carbon restructuring, and microbial functional potential observed in this field experiment illustrates how soil systems organize methane-processing potential following a point-source emission. Although subsurface soils at METEC were methane-saturated, strong vertical attenuation produced steep redox and concentration gradients in overlying horizons, consistent with diffusion constraints documented previously at this site.[42] This vertical attenuation generated a near-surface CH_4−O_2 boundary where methane availability, reconstructed oxygen availability, carbonate-isotope structure, and C_1 functional potential converged. The alignment of these features identifies this boundary as the interval most consistent with aerobic oxidation potential and carbon-pool transformation in upland soils.[43]

Isotopic and stoichiometric patterns revealed plume-scale restructuring of solid-phase carbon pools across the methane gradient. Although these signatures are composite rather than uniquely diagnostic of any single process, especially in the absence of isotope characterization of the injected gas, their spatial organization indicates that methane exposure was associated with differences in both organic and inorganic carbon pools. At the CH_4-saturated, O_2-limited plume center, acid-rinsed organic $\delta^{13}C$ enrichment and elevated C:N ratios coincided with high carbonate abundance and carbonate $\delta^{13}C$ values near −4.5‰, supporting carbonate accumulation under methane-influenced carbon-release conditions.[44] With increasing distance from the plume center, carbonate-specific $\delta^{13}C$−$\delta^{18}O$ compositions resolved an intermediate geochemical transition between the carbonate-rich plume center and distal low-carbonate soils. Acid-rinsed organic $\delta^{13}C$ did not resolve the same intermediate structure, instead occupying a broader overlapping range outside the plume center. This divergence between carbonate and organic isotope patterns is consistent with isotopic hysteresis in bulk soil organic matter: organic $\delta^{13}C$ integrates over prior carbon inputs, whereas newly formed carbonate in an otherwise noncalcareous soil can more closely track short-term changes in pore-gas chemistry over a two-day release interval. Thus, solid-phase $\delta^{13}C$ in methane-influenced soils reflects the integrated effects of CO_2/DIC source mixing, methane oxidation, carbonate precipitation, transport, and organic matter turnover rather than a single source endmember.[28,29,31,45,46]

In parallel, microbial functional profiles identify the CH_4−O_2 boundary as the interval where aerobic methane and short-chain hydrocarbon oxidation potential was most strongly enriched and coordinated. Near this boundary and the associated geochemical transition zone, monooxygenase genes were locally enriched and covaried with C_1 uptake and assimilation pathways. In contrast, the CH_4-saturated plume center showed the strongest solid-phase carbon signal but not the strongest aerobic C_1 functional enrichment, consistent with

Downloaded from pubs.acs.org/esthag/article-pdf/60/32/22397/6456396/acs.est.6c03515.pdf by guest on 19 August 2026

https://doi.org/10.1021/acs.est.6c03515
Environ. Sci. Technol. 2026, 60, 22397−22407

O_2 limitation under gas-saturated conditions. This pattern indicates coordinated C_1-processing potential within hydrocarbon-oxidizing functional guilds in the resident soil community, including lineages with preexisting monooxygenase repertoires, without broad turnover of the heterotrophic assemblage. The single day 2 microbial sampling point limits attribution of this functional organization to growth during the release, as opposed to oxidative capacity shaped by prior methane exposure at the test bed. Nevertheless, the alignment among redox gradients, carbonate-isotope patterns, monooxygenase abundance, and C_1 assimilation markers indicates that diffusion-controlled distributions of CH_4−O_2 availability organized methane-oxidation-related functional potential across the gradient. Although transient microsites may have supported microaerobic or alternative anaerobic pathways,[47−49] including processes described in seep and wetland systems,[50,51] aerobic C_1 metabolism was the primary methane-responsive functional signal in the sampled near-surface soils.

Genome-resolved analyses linked this localized functional enrichment to actinobacterial lineages encoding monooxygenases within the CH_4−O_2 overlap zone, a pattern consistent across gene-centric and MAG-level analyses. This lineage-level signal is notable because recent studies have documented methane oxidation capacity in actinobacterial lineages from hydrocarbon-rich and upland environments,[39−41,52,53] expanding the recognized phylogenetic breadth of methane-oxidizing taxa. This pattern also aligns with evolutionary evidence that soluble methane monooxygenases arose from ancestral C_2−C_4 alkane monooxygenases,[54] suggesting that broad oxidative repertoires may facilitate facultative responses to transient methane and hydrocarbon exposure. Such metabolic flexibility may be especially advantageous in heterotrophic soils exposed to transient methane inputs, where persistence between pulses likely depends on access to SOC-derived substrates. Although canonical methanotrophs may also have contributed, the predominance of Actinomycetota is consistent with environmental filtering for facultative, broad-substrate oxidizers under transient methane exposure. The spatial enrichment of these operons may therefore reflect a combination of prior selection at the test bed, preexisting facultative oxidative capacity, and short-term organization of that capacity along the day 2 CH_4−O_2 boundary. Thus, facultative lineages with broad substrate ranges may expand the biological capacity for methane and short-chain hydrocarbon oxidation during transient methane pulses, alongside canonical methanotrophs.

Taken together, these findings support a model in which methane attenuation potential in upland soils is organized around a spatially restricted CH_4−O_2 interface that is not simply a transition between plume center and distal soils, but a biogeochemical boundary where methane transport, carbonate restructuring, and biological oxidation potential converge. Field studies of methane leakage from compromised or abandoned wells similarly show that soil-mediated oxidation can regulate surface methane emissions,[28,29] highlighting near-surface soils as dynamic methane filters whose attenuation capacity depends on leak geometry, oxygen availability, and soil structure. Future work integrating transcriptomics, direct flux measurements, and longer-term monitoring will be needed to quantify how gene expression, methane consumption, and carbonate dynamics covary across shifting moisture and diffusion conditions. Incorporating spatially explicit microbial processes and redox-boundary structure into emission models may improve predictions of soil-mediated methane attenuation,[55,56] although direct rate and flux measurements will be required for quantitative parametrization.

MATERIALS AND METHODS

Field Experiment and Sample Collection

A controlled natural gas release experiment was conducted in June 2023 at Colorado State University's Methane Emissions Technology Evaluation Center (METEC), an outdoor facility in Fort Collins, Colorado, designed to simulate underground pipeline leaks. The experiment used a 5.5 × 5.5 m grass-covered sandy-loam testbed instrumented for continuous methane, moisture, and temperature monitoring (Figure S1). The upper 1 m showed no observable stratification and was treated as spatially homogeneous for pore-gas reconstruction. Testing occurred approximately 2.5 years after testbed construction; reported soil properties included a porosity of 0.45 cm^3 cm^{-3}, permeability of 2.18 × 10^{-13} m^2, and organic content <5%.[42,57−59]

The natural gas source was positioned 0.9 m below ground surface (BGS) beneath a 2-in. diameter PVC pipe used to simulate a distribution pipeline. Gas was delivered through 0.635 cm PTFE tubing to a vent screen enclosed within a gravel-filled 10 cm wire-mesh cube. The released mixture contained approximately 85−95% methane, up to ∼10% ethane, and balance air. Flow was maintained at 10 standard liters per minute (20 scfh) for five days using pressure regulators, solenoid valves, and precision orifices; monitoring continued through day 7.

Subsurface methane, soil moisture, and temperature were monitored at radial distances of 0, 1.3, 3.2, and 4.6 m and depths of 0.01, 0.1, 0.3, 0.6, and 0.9 m BGS (Figure 1A; Figure S1). Methane concentrations were recorded every 5 s with SGX INIR-ME100 sensors (SGX Sensortech, Corcelles-Cormondrèche, Switzerland), and colocated TEROS 10/11 sensors (METER Group, Pullman, WA, USA) recorded moisture and temperature every 10 min. Surface methane was mapped in each cardinal direction at 0.5 m intervals to 5 m using a Gas Rover detector (Bascom Turner Inc., Norwood, MA, USA). Background atmospheric methane concentrations were measured approximately 1 m aboveground and upwind using a mid-infrared laser absorption spectrometer (MIRA Strato LDS, Aeris Technologies, Hayward, CA, USA) and ranged from 1.95 to 2.3 ppm.[60] Additional details on METEC testbed construction and sensor deployment are described previously.[42,58]

Surface soils were collected after approximately two days of release, once subsurface and near-surface methane measurements indicated that the plume had reached a quasi-steady spatial structure (Figure S2). Prerelease soil sampling was not possible because of safety restrictions at the active controlled-release field site. During the release, soil collection was further restricted to locations without embedded sensors or release infrastructure. Samples were therefore collected from accessible, noninstrumented locations at radial distances of 0, 1.25, 2.5, 3.75, and 5 m in each cardinal direction from the release point (N = 34 total). Continuous gas sensors and soil samples were not perfectly colocated; thus, spatial correspondence between gas gradients and soil geochemical or microbial patterns was interpreted as approximate radial alignment rather than exact colocation. The 5 m samples were treated as distal reference soils for the sampled surface gradient, rather than as a demonstrated prerelease baseline, based on the decline of surface CH_4 concentrations below detector threshold beyond 3.5 m.

Sampling tools were disinfected with 70% ethanol between locations, and gloves were replaced between samples. Soils were collected in sterile Whirl-Pak bags, transported on dry ice, stored at −80 °C, and homogenized before geochemical analysis and DNA extraction.

Pore-Gas Modeling and Calculations

Atmospheric forcing, soil physical properties, and pore connectivity can ventilate the upper soil profile to depths ranging from several tens of centimeters to approximately 1 m.[61,62] We therefore integrated

Downloaded from pubs.acs.org/esthag/article-pdf/60/32/22397/6456396/acs.est.6c03515.pdf by guest on 19 August 2026

https://doi.org/10.1021/acs.est.6c03515
Environ. Sci. Technol. 2026, 60, 22397−22407

methane, moisture, and temperature measurements to estimate pore-gas CH_4 and first-order O_2 availability during the release.

Soil volumetric water content (θ, $cm^3\ cm^{-3}$) was paired with CH_4 measurements using nearest-time matching (±30 s). Degree of saturation (S) and gas-filled porosity (ϕ_g) were calculated at each depth as:

$$S = \frac{\theta}{\phi}, \quad \phi_g = \phi(1 - S)$$

where total porosity (ϕ) was assumed to be 0.45 $cm^3\ cm^{-3}$, based on representative values for METEC testbed soils.

The gas-phase O_2 mole fraction was estimated assuming that methane displaced atmospheric gases proportionally:

$$f_{O_2} = 0.2095(1 - f_{CH_4})$$

where 0.2095 represents the atmospheric O_2 mole fraction. This formulation assumes negligible accumulation of other gases and provides a first-order estimate of potential O_2 availability under methane enrichment rather than direct pore-gas measurements. This first-order estimate does not account for other injected hydrocarbons, species-specific diffusivities, biological O_2 consumption, or microscale pore heterogeneity, which could shift the position or thickness of the inferred CH_4–O_2 overlap zone.

Bulk-soil gas concentrations (mol m^{-3} soil) were calculated using the molar density of air at ambient conditions (41 mol m^{-3}) scaled by gas-filled porosity. Modeled pore-gas CH_4 and reconstructed O_2 concentrations were extracted at 0.01 and 0.1 m BGS for the time point corresponding to soil sampling (day 2) and used to infer the spatial extent of the CH_4–O_2 overlap zone.

Soil Stable Isotope and Geochemical Analyses

Soil carbon and nitrogen contents and stable isotope compositions were measured by elemental analysis–isotope ratio mass spectrometry. To evaluate carbonate contributions to bulk-soil signatures, samples were analyzed without pretreatment, after HCl rinsing, and after HCl fumigation. Carbonate-specific $\delta^{13}C$ and $\delta^{18}O$ values were measured separately by phosphoric acid digestion and GasBench–IRMS. Isotope values were calibrated to international and in-house standards, with analytical precision <0.1‰ for carbonate $\delta^{13}C$ and $\delta^{18}O$. The injected natural gas was not isotopically characterized during this release; therefore, solid-phase $\delta^{13}C$ values were not used to quantify methane-derived carbon incorporation or perform source-gas attribution. Detailed sample preparation, calibration, and analytical procedures are provided in the Supporting Information.

Metagenomic Data Processing

Sample Preparation. DNA was extracted from 0.05 g of surface soils using the ZymoBIOMICS 96 DNA Kit and sequenced on an Illumina NovaSeq 6000 platform using 150 bp paired-end reads. Reads were quality filtered with the BBMap v38.96 toolkit.[63] For gene-centric analyses, merged reads and unmerged forward reads were retained to represent each original paired-end fragment once and avoid double-counting. For assembly based analyses, merged reads and both members of unmerged pairs were retained, preserving the complete quality-filtered read set. Detailed extraction, library preparation, and read-processing procedures are provided in the Supporting Information.

Taxonomic and Broad Functional Composition. Taxonomic composition was estimated using phylogenetic inference of reads assigned to curated single-copy marker genes,[64] as previously described.[65] Relative-abundance matrices were Hellinger transformed, and Bray–Curtis dissimilarities were visualized by nonmetric multidimensional scaling. Effects of distance and cardinal direction were evaluated using PERMANOVA and PERMDISP with permutations blocked by transect; observed richness, Shannon diversity, and Simpson diversity were also calculated.

Broad functional composition was quantified from PfamA v37 protein-family annotations[66] normalized to counts per million (CPM) total PFAM hits. Annotations were evaluated across all protein families, glycoside hydrolases and carbohydrate-binding modules, and curated primary-metabolism pathways. Community-level patterns were analyzed using Bray–Curtis ordination, PERMANOVA, and PERMDISP. Distance-responsive functional categories were tested using linear models and quasibinomial generalized linear models with 5 m samples as the distal reference. Detailed databases, software, and statistical procedures are provided in the Supporting Information.

C_1 Functional Pathways. Custom HMMs[67] were constructed from KEGG orthologs[68] and curated reference sequences[69] for methane oxidation and downstream C_1 metabolism (Table S3). Translated, unassembled reads were screened using fragment-aware alignment and score filters, with the highest-scoring model retained per read. Accessory genes were counted only when supporting pathway markers occurred in the same sample. Gene counts were normalized to total PFAM annotations and evaluated across sampling radii using Kruskal–Wallis tests, Spearman rank correlations, linear models, and hierarchical clustering.

These analyses were designed to quantify C_1 metabolic potential at the pathway/module level. Because homologous methane, ammonia, and broader hydrocarbon monooxygenase families cannot always be resolved from short fragments, monooxygenase hits were interpreted as putative *mmoX*/SDIMO and *pmoA*/*amoA* marker-family assignments. Taxonomy was assigned from DIAMOND[70] searches against NCBI nr and summarized from classified hits. These taxonomic assignments were made from unassembled monooxygenase reads rather than complete, taxonomically resolved genomes; accordingly, we did not calculate alpha diversity for a putative methanotrophic subset. Full HMM construction, filtering, pathway-support rules, and statistical procedures are provided in the Supporting Information.

Metagenome-Assembled Genome Recovery. Complete quality-filtered read sets were pooled by radial distance and assembled with MEGAHIT v1.2.9.[71] Reads were not k-mer normalized because most unique k-mers were singletons and normalization would have disproportionately removed low-abundance functional genes. Contigs were binned using differential coverage and an ensemble of complementary binning methods. Genome bins were quality assessed, dereplicated across distance-specific assemblies, taxonomically classified using GTDB-Tk v2.4.0,[72] and functionally annotated with DRAM v1.5.0.[73] Detailed assembly, mapping, binning, and genome-quality procedures are provided in the Supporting Information.

Identification of MMO Operons. MAG-associated contigs were screened for methane and related hydrocarbon monooxygenase operons. Candidate operons required at least three colocalized monooxygenase genes within 5 kbp and a catalytic subunit, either *mmoX* for SDIMOs or *pmoA*/*amoA* for CuMMOs. Candidate sequences required concordant DIAMOND and HMM evidence and were classified through catalytic-subunit phylogenies containing characterized methane, ammonia, and hydrocarbon monooxygenases. Operon architecture, conserved Cu_B/Cu_C residues, and AlphaFold-based protein modeling provided additional support for CuMMO classification.

Operon abundance was quantified by mapping quality-filtered paired reads to monooxygenase-containing contigs and normalizing mean contig coverage to median coverage of quality-filtered single-copy marker genes from the same assemblies. This genome-equivalent normalization controlled for sample-level differences in sequencing depth and assembly recovery. Complete database construction, phylogenetic, structural, mapping, and normalization procedures are provided in the Supporting Information.

All statistical analyses were performed in R v4.2.2.

■ ASSOCIATED CONTENT

Data Availability Statement

Paired-end shotgun metagenomic data were deposited in the NCBI Sequence Read Archive under the BioProject PRJNA1465354. All other data, scripts, and HMM thresholds are available in the Supporting Information and on GitHub (https://github.com/alex-b-chase/metec-NGleak).

Downloaded from pubs.acs.org/esthag/article-pdf/60/32/22397/6456396/acs.est.6c03515.pdf by guest on 19 August 2026

https://doi.org/10.1021/acs.est.6c03515
Environ. Sci. Technol. 2026, 60, 22397–22407

Supporting Information

The Supporting Information is available free of charge at https://pubs.acs.org/doi/10.1021/acs.est.6c03515.

Supplemental methods, supplementary figures (S1−S15), and tables (S1−S3) (PDF)

AUTHOR INFORMATION

Corresponding Author

Alexander B. Chase − *Department of Earth Sciences, Southern Methodist University, Dallas, Texas 75205, United States;* orcid.org/0000-0003-1984-6279; Email: abchase@smu.edu

Authors

J.R.R. Navodi Jayarathne − *Department of Civil and Environmental Engineering, Southern Methodist University, Dallas, Texas 75205, United States;* orcid.org/0000-0003-1515-0290

Motahare Haghighatjoo − *Department of Earth Sciences, Southern Methodist University, Dallas, Texas 75205, United States*

Neil J. Tabor − *Department of Earth Sciences, Southern Methodist University, Dallas, Texas 75205, United States*

Kathleen M. Smits − *Department of Civil and Environmental Engineering, Southern Methodist University, Dallas, Texas 75205, United States;* orcid.org/0000-0002-8319-0940

Complete contact information is available at: https://pubs.acs.org/10.1021/acs.est.6c03515

Author Contributions

A.B.C. and K.M.S. designed the research; A.B.C., J.R.R.N.J., and N.J.T. performed the research; A.B.C., J.R.R.N.J., M.H., and N.J.T. analyzed the data; and A.B.C. wrote the paper with input from all authors.

Funding

This work was supported by the U.S. Department of Transportation Pipeline and Hazardous Materials Safety Administration (PHMSA) under Grant No. 693JK32010011POTA to K.S.M. and generous start-up funds from SMU to A.B.C.

Notes

The authors declare no competing financial interest.

ACKNOWLEDGMENTS

We thank Claudia Weihe from UC Irvine and John Robbins from the SMU Stable Isotope Lab for assistance with sample processing, the UC Irvine Genomics Research and Technology Hub for metagenomic sequencing, and the SMU M3 high-performance computing for computational resources. The authors declare that there is no conflict of interest regarding the publication of this article.

REFERENCES

(1) Allen, G. Rebalancing the Global Methane Budget. *Nature* **2016**, *538* (7623), 46−48.

(2) Aronson, E. L.; Allison, S. D.; Helliker, B. R. Environmental Impacts on the Diversity of Methane-Cycling Microbes and Their Resultant Function. *Front. Microbiol.* **2013**, *4*, 225.

(3) Riley, W. J.; Subin, Z. M.; Lawrence, D. M.; Swenson, S. C.; Torn, M. S.; Meng, L.; Mahowald, N. M.; Hess, P. Barriers to Predicting Changes in Global Terrestrial Methane Fluxes: Analyses Using CLM4Me, a Methane Biogeochemistry Model Integrated in CESM. *Biogeosciences* **2011**, *8* (7), 1925−1953.

(4) Dutaur, L.; Verchot, L. V.A Global Inventory of the Soil CH4 Sink.*Global Biogeochem. Cycles***2007***214*

(5) Saunois, M.; Stavert, A. R.; Poulter, B.; Bousquet, P.; Canadell, J. G.; Jackson, R. B.; Raymond, P. A.; Dlugokencky, E. J.; Houweling, S.; Patra, P. K.; et al. The Global Methane Budget 2000−2017. *Earth Syst. Sci. Data* **2020**, *12* (3), 1561−1623.

(6) Conrad, R. The Global Methane Cycle: Recent Advances in Understanding the Microbial Processes Involved. *Environ. Microbiol. Rep.* **2009**, *1* (5), 285−292.

(7) Bahlmann, L. M.; Smits, K. M.; Heck, K.; Coltman, E.; Helmig, R.; Neuweiler, I. Gas Component Transport across the Soil-atmosphere Interface for Gases of Different Density: Experiments and Modeling. *Water Resour. Res.* **2020**, *56* (9), No. e2020WR027600.

(8) Ulrich, B. A.; Mitton, M.; Lachenmeyer, E.; Hecobian, A.; Zimmerle, D.; Smits, K. M. Natural Gas Emissions from Underground Pipelines and Implications for Leak Detection. *Environ. Sci. Technol. Lett.* **2019**, *6* (7), 401−406.

(9) Sulman, B. N.; Moore, J. A. M.; Abramoff, R.; Averill, C.; Kivlin, S.; Georgiou, K.; Sridhar, B.; Hartman, M. D.; Wang, G.; Wieder, W. R.; et al. Multiple Models and Experiments Underscore Large Uncertainty in Soil Carbon Dynamics. *Biogeochemistry* **2018**, *141* (2), 109−123.

(10) Sokol, N. W.; Slessarev, E.; Marschmann, G. L.; Nicolas, A.; Blazewicz, S. J.; Brodie, E. L.; Firestone, M. K.; Foley, M. M.; Hestrin, R.; Hungate, B. A.; et al. Life and Death in the Soil Microbiome: How Ecological Processes Influence Biogeochemistry. *Nat. Rev. Microbiol.* **2022**, *20* (7), 415−430.

(11) Wieder, W. R.; Bonan, G. B.; Allison, S. D. Global Soil Carbon Projections Are Improved by Modelling Microbial Processes. *Nat. Clim. Change* **2013**, *3* (10), 909−912.

(12) Li, Z.; Riley, W. J.; Marschmann, G. L.; Karaoz, U.; Shirley, I. A.; Wu, Q.; Bouskill, N. J.; Chang, K.-Y.; Crill, P. M.; Grant, R. F.; et al. A Framework for Integrating Genomics, Microbial Traits, and Ecosystem Biogeochemistry. *Nat. Commun.* **2025**, *16* (1), 2186.

(13) Abs, E.; Chase, A. B.; Allison, S. D. How Do Soil Microbes Shape Ecosystem Biogeochemistry in the Context of Global Change? *Environ. Microbiol.* **2023**, *25*, 780−785.

(14) Pratscher, J.; Vollmers, J.; Wiegand, S.; Dumont, M. G.; Kaster, A. Unravelling the Identity, Metabolic Potential and Global Biogeography of the Atmospheric Methane-oxidizing Upland Soil Cluster α. *Environ. Microbiol.* **2018**, *20* (3), 1016−1029.

(15) Knief, C.; Lipski, A.; Dunfield, P. F. Diversity and Activity of Methanotrophic Bacteria in Different Upland Soils. *Appl. Environ. Microbiol.* **2003**, *69* (11), 6703−6714.

(16) Dedysh, S. N. Exploring Methanotroph Diversity in Acidic Northern Wetlands: Molecular and Cultivation-Based Studies. *Microbiology* **2009**, *78* (6), 655−669.

(17) Lee, H. J.; Jeong, S. E.; Kim, P. J.; Madsen, E. L.; Jeon, C. O. High Resolution Depth Distribution of Bacteria, Archaea, Methanotrophs, and Methanogens in the Bulk and Rhizosphere Soils of a Flooded Rice Paddy. *Front. Microbiol.* **2015**, *6*, 639.

(18) Singleton, C. M.; McCalley, C. K.; Woodcroft, B. J.; Boyd, J. A.; Evans, P. N.; Hodgkins, S. B.; Chanton, J. P.; Frolking, S.; Crill, P. M.; Saleska, S. R.; et al. Methanotrophy across a Natural Permafrost Thaw Environment. *ISME J.* **2018**, *12* (10), 2544−2558.

(19) Hanson, R. S.; Hanson, T. E. Methanotrophic Bacteria. *Microbiol Rev.* **1996**, *60* (2), 439−471.

(20) Knief, C. Diversity and Habitat Preferences of Cultivated and Uncultivated Aerobic Methanotrophic Bacteria Evaluated Based on PmoA as Molecular Marker. *Front. Microbiol.* **2015**, *6*, 1346.

(21) Khadka, R.; Clothier, L.; Wang, L.; Lim, C. K.; Klotz, M. G.; Dunfield, P. F. Evolutionary History of Copper Membrane Monooxygenases. *Front. Microbiol.* **2018**, *9*, 2493.

(22) Kalyuzhnaya, M. G.; Lapidus, A.; Ivanova, N.; Copeland, A. C.; McHardy, A. C.; Szeto, E.; Salamov, A.; Grigoriev, I. V.; Suciu, D.; Levine, S. R.; et al. High-Resolution Metagenomics Targets Specific

Downloaded from pubs.acs.org/esthag/article-pdf/60/32/22397/6456396/acs.est.6c03515.pdf by guest on 19 August 2026

Functional Types in Complex Microbial Communities. *Nat. Biotechnol.* **2008**, *26* (9), 1029−1034.
(23) Crombie, A. T.; Khawand, M. E.; Rhodius, V. A.; Fengler, K. A.; Miller, M. C.; Whited, G. M.; McGenity, T. J.; Murrell, J. C. Regulation of Plasmid-encoded Isoprene Metabolism in *Rhodococcus*, a Representative of an Important Link in the Global Isoprene Cycle. *Environ. Microbiol.* **2015**, *17* (9), 3314−3329.
(24) Op den Camp, H. J. M.; Islam, T.; Stott, M. B.; Harhangi, H. R.; Hynes, A.; Schouten, S.; Jetten, M. S. M.; Birkeland, N.; Pol, A.; Dunfield, P. F. Environmental, Genomic and Taxonomic Perspectives on Methanotrophic Verrucomicrobia. *Environ. Microbiol. Rep.* **2009**, *1* (5), 293−306.
(25) Gwak, J.-H.; Awala, S. I.; Nguyen, N.-L.; Yu, W.-J.; Yang, H.-Y.; von Bergen, M.; Jehmlich, N.; Kits, K. D.; Loy, A.; Dunfield, P. F.; et al. Sulfur and Methane Oxidation by a Single Microorganism. *Proc. Natl. Acad. Sci. U. S. A.* **2022**, *119*, No. e2114799119.
(26) Mayr, M. J.; Parra, S. A.; Connon, S. A.; Narayanan, A. K.; Murali, R.; Crémière, A.; Orphan, V. J. Distinct Microbial Communities within and on Seep Carbonates Support Long-Term Anaerobic Oxidation of Methane and Divergent pMMO Diversity. *ISME J.* **2025**, *19* (1), wraf153.
(27) EPA, U.S. *Inventory of US Greenhouse Gas Emissions and Sinks: 1990−2017*; US Environmental Protection Agency, 2019.
(28) Cahill, A. G.; McClure, J.; de Jonge-Anderson, I. Natural Soils-based Oxidation Mitigates Methane Leakage from Integrity Compromised Legacy Wells. *Geophys. Res. Lett.* **2025**, *52* (5), No. e2024GL113522.
(29) Schout, G.; Griffioen, J.; Hassanizadeh, S. M.; de Lichtbuer, G. C.; Hartog, N. Occurrence and Fate of Methane Leakage from Cut and Buried Abandoned Gas Wells in the Netherlands. *Sci. Total Environ.* **2019**, *659*, 773−782.
(30) Shi, L.-D.; Guo, T.; Lv, P.-L.; Niu, Z.-F.; Zhou, Y.-J.; Tang, X.-J.; Zheng, P.; Zhu, L.-Z.; Zhu, Y.-G.; Kappler, A.; et al. Coupled Anaerobic Methane Oxidation and Reductive Arsenic Mobilization in Wetland Soils. *Nat. Geosci.* **2020**, *13* (12), 799−805.
(31) Jordan, S. F. A.; Schloemer, S.; Krüger, M.; Heffner, T.; Horn, M. A.; Blumenberg, M. Interferences Caused by the Biogeochemical Methane Cycle in Peats during the Assessment of Abandoned Oil Wells. *Biogeosciences* **2025**, *22* (3), 809−830.
(32) Megonigal, J. P.; Hines, M. E.; Visscher, P. T. Anaerobic Metabolism: Linkages to Trace Gases and Aerobic Processes. *Treatise on Geochemistry*; Elsevier, 2003; Vol. *8*, pp 317−424.
(33) Okamoto, H.; Gomi, Y. Empirical Research on Diffusion Behavior of Leaked Gas in the Ground. *J. Loss Prev. Process Ind* **2011**, *24* (5), 531−540.
(34) Young, A. The Effects of Fluctuations in Atmospheric Pressure on Landfill Gas Migration and Composition. *Water, Air, Soil Pollut.* **1992**, *64*, 601−616.
(35) Hibi, Y.; Kanou, Y.; Ohira, Y. Estimation of Mechanical Dispersion and Dispersivity in a Soil−Gas System by Column Experiments and the Dusty Gas Model. *J. Contam. Hydrol.* **2012**, *131* (1−4), 39−53.
(36) Liew, E. F.; Tong, D.; Coleman, N. V.; Holmes, A. J. Mutagenesis of the Hydrocarbon Monooxygenase Indicates a Metal Centre in Subunit-C, and Not Subunit-B, Is Essential for Copper-Containing Membrane Monooxygenase Activity. *Microbiology* **2014**, *160* (6), 1267−1277.
(37) Ross, M. O.; MacMillan, F.; Wang, J.; Nisthal, A.; Lawton, T. J.; Olafson, B. D.; Mayo, S. L.; Rosenzweig, A. C.; Hoffman, B. M. Particulate Methane Monooxygenase Contains Only Mononuclear Copper Centers. *Science* **2019**, *364* (6440), 566−570.
(38) Yang, S. N. N.; Kertesz, M. A.; Coleman, N. V. Phylogenetic and Functional Diversity of Soluble Di-Iron Monooxygenases. *Environ. Microbiol.* **2025**, *27* (2), No. e70050.
(39) Kambara, H.; Kawamoto, T.; Matsushita, S.; Kindaichi, T.; Ozaki, N.; Aoi, Y.; Takaki, Y.; Imachi, H.; Nobu, M. K.; Ogawara, M.; et al. First isolation of a methanotrophic *Mycobacterium* reveals ammonia- and pH-tolerant methane oxidation. *Appl. Environ. Microbiol.* **2025**, *91* (8), No. e00796−25.
(40) Coleman, N. V.; Yau, S.; Wilson, N. L.; Nolan, L. M.; Migocki, M. D.; Ly, M.; Crossett, B.; Holmes, A. J. Untangling the Multiple Monooxygenases of *Mycobacterium chubuense* Strain NBB4, a Versatile Hydrocarbon Degrader. *Environ. Microbiol. Rep.* **2011**, *3* (3), 297−307.
(41) Van Spanning, R. J. M.; Guan, Q.; Melkonian, C.; Gallant, J.; Polerecky, L.; Flot, J.-F.; Brandt, B. W.; Braster, M.; Espinoza, P. I.; Aerts, J. W.; et al. Methanotrophy by a *Mycobacterium* Species That Dominates a Cave Microbial Ecosystem. *Nat. Microbiol.* **2022**, *7* (12), 2089−2100.
(42) Jayarathne, J. R. R. N.; Smits, K. M.; Riddick, S. N.; Zimmerle, D. *Understanding of the Degree to Which Parameters Affect the Subsurface Natural Gas Migration with Significant Flow Rates*; Pipeline and Hazardous Materials Safety Administration: Washington, D.C, 2024
(43) Etiope, G.; Klusman, R. W. Methane Microseepage in Drylands: Soil Is Not Always a CH4 Sink. *J. Integr. Environ. Sci.* **2010**, *7* (S1), 31−38.
(44) Frieling, J.; Svensen, H. H.; Planke, S.; Cramwinckel, M. J.; Selnes, H.; Sluijs, A. Thermogenic Methane Release as a Cause for the Long Duration of the PETM. *Proc. Natl. Acad. Sci. U. S. A.* **2016**, *113* (43), 12059−12064.
(45) Cerling, T. E. The Stable Isotopic Composition of Modern Soil Carbonate and Its Relationship to Climate. *Earth Planet. Sci. Lett.* **1984**, *71* (2), 229−240.
(46) Marlow, J. J.; Steele, J. A.; Ziebis, W.; Thurber, A. R.; Levin, L. A.; Orphan, V. J. Carbonate-Hosted Methanotrophy Represents an Unrecognized Methane Sink in the Deep Sea. *Nat. Commun.* **2014**, *5* (1), 5094.
(47) Chamberlain, S. D.; Gomez-Casanovas, N.; Walter, M. T.; Boughton, E. H.; Bernacchi, C. J.; DeLucia, E. H.; Groffman, P. M.; Keel, E. W.; Sparks, J. P. Influence of Transient Flooding on Methane Fluxes from Subtropical Pastures. *J. Geophys. Res. Biogeosci.* **2016**, *121* (3), 965−977.
(48) Noël, V.; Boye, K.; Naughton, H. R.; Lacroix, E. M.; Aeppli, M.; Kumar, N.; Fendorf, S.; Webb, S. M. X-Ray Chemical Imaging for Assessing Redox Microsites within Soils and Sediments. *Front. Environ. Chem.* **2024**, *5*, 1329887.
(49) Deutzmann, J. S.; Stief, P.; Brandes, J.; Schink, B. Anaerobic Methane Oxidation Coupled to Denitrification Is the Dominant Methane Sink in a Deep Lake. *Proc. Natl. Acad. Sci. U. S. A.* **2014**, *111* (51), 18273−18278.
(50) Mohanty, S. R.; Bodelier, P. L. E.; Floris, V.; Conrad, R. Differential Effects of Nitrogenous Fertilizers on Methane-Consuming Microbes in Rice Field and Forest Soils. *Appl. Environ. Microbiol.* **2006**, *72* (2), 1346−1354.
(51) Reay, D. S.; Nedwell, D. B.; McNamara, N.; Ineson, P. Effect of Tree Species on Methane and Ammonium Oxidation Capacity in Forest Soils. *Soil Biol. Biochem.* **2005**, *37* (4), 719−730.
(52) Farhan Ul Haque, M.; Hernández, M.; Crombie, A. T.; Murrell, J. C. Identification of Active Gaseous-Alkane Degraders at Natural Gas Seeps. *ISME J.* **2022**, *16* (7), 1705−1716.
(53) Farhan Ul Haque, M.; Crombie, A. T.; Murrell, J. C. Novel Facultative *Methylocella* Strains Are Active Methane Consumers at Terrestrial Natural Gas Seeps. *Microbiome* **2019**, *7* (1), 134.
(54) Osborne, C. D.; Haritos, V. S. Beneath the Surface: Evolution of Methane Activity in the Bacterial Multicomponent Monooxygenases. *Mol. Phylogenet. Evol.* **2019**, *139*, 106527.
(55) Abs, E.; Chase, A. B.; Manzoni, S.; Ciais, P.; Allison, S. D. Microbial evolution—An under-appreciated driver of soil carbon cycling. *Glob Chang Biol.* **2024**, *30* (4), No. e17268.
(56) Abs, E.; Keuschnig, C.; Amato, P.; Bowler, C.; Capo, E.; Chase, A. B.; Chavez Rodriguez, L.; Dabengwa, A.; Dussarrat, T.; Guzman, T.; et al. Ideas and Perspectives: Using Meta-Omics to Unravel Biogeochemical Changes from Cell to Planetary Scales. *Biogeosciences* **2026**, *23*, 5205−5237.
(57) Mitton, M. *Subsurface Methane Migration from Natural Gas Distribution Pipelines as Affected by Soil Heterogeneity: Field Scale Experimental and Numerical Study*; Colorado School of Mines, 2018.

Downloaded from pubs.acs.org/esthag/article-pdf/60/32/22397/6456396/acs.est.6c03515.pdf by guest on 19 August 2026

(58) Jayarathne, J. R. R. N.; Zimmerle, D.; Kolodziej, R. S.; Riddick, S.; Smits, K. M. Flow and Transport of Methane from Leaking Underground Pipelines: Effects of Soil Surface Conditions and Implications for Natural Gas Leak Classification. *Environ. Sci. Technol. Lett.* **2024**, *11* (6), 539−545.
(59) Cho, Y.; Ulrich, B. A.; Zimmerle, D. J.; Smits, K. M. Estimating Natural Gas Emissions from Underground Pipelines Using Surface Concentration Measurements. *Environ. Pollut.* **2020**, *267*, 115514.
(60) Kolodziej, R. S., IV; Gundapuneni, V. R.; Jayarathne, J. R. R. N.; Tian, S.; Zimmerle, D. J.; Smits, K. M. Impacts of Mixed Hydrocarbon Compositions on the Probability of Detection of Belowground Pipeline Leaks Using Mobile Survey Methods. *Elem Sci. Anth.* **2026**, *14* (1), 00011.
(61) Maier, M.; Schack-Kirchner, H.; Aubinet, M.; Goffin, S.; Longdoz, B.; Parent, F. Turbulence Effect on Gas Transport in Three Contrasting Forest Soils. *Soil Sci. Soc. Am. J.* **2012**, *76* (5), 1518−1528.
(62) Takle, E. S.; Massman, W. J.; Brandle, J. R.; Schmidt, R. A.; Zhou, X.; Litvina, I. V.; Garcia, R.; Doyle, G.; Rice, C. W. Influence of High-Frequency Ambient Pressure Pumping on Carbon Dioxide Efflux from Soil. *Agric. For. Meteorol.* **2004**, *124* (3−4), 193−206.
(63) Bushnell, B. *BBMap: A Fast, Accurate, Splice-Aware Aligner*; Lawrence Berkeley National Lab.(LBNL): Berkeley, CA, United States, 2014.
(64) Wu, D.; Jospin, G.; Eisen, J. A. Systematic Identification of Gene Families for Use as "Markers" for Phylogenetic and Phylogeny-Driven Ecological Studies of Bacteria and Archaea and Their Major Subgroups. *PLoS One* **2013**, *8* (10), No. e77033.
(65) Chase, A. B.; Gomez-Lunar, Z.; Lopez, A. E.; Li, J.; Allison, S. D.; Martiny, A. C.; Martiny, J. B. H. Emergence of Soil Bacterial Ecotypes along a Climate Gradient. *Environ. Microbiol.* **2018**, *20* (11), 4112−4126.
(66) Finn, R. D.; Bateman, A.; Clements, J.; Coggill, P.; Eberhardt, R. Y.; Eddy, S. R.; Heger, A.; Hetherington, K.; Holm, L.; Mistry, J.; et al. Pfam: The Protein Families Database. *Nucleic Acids Res.* **2014**, *42* (D1), D222−D230.
(67) Johnson, L. S.; Eddy, S. R.; Portugaly, E. Hidden Markov Model Speed Heuristic and Iterative HMM Search Procedure. *BMC Bioinf.* **2010**, *11* (1), 431.
(68) Aoki-Kinoshita, K. F.; Kanehisa, M. Gene Annotation and Pathway Mapping in KEGG. In *Comparative genomics*; Springer, 2007; pp. 71−91.
(69) Lavy, A.; McGrath, D. G.; Matheus Carnevali, P. B.; Wan, J.; Dong, W.; Tokunaga, T. K.; Thomas, B. C.; Williams, K. H.; Hubbard, S. S.; Banfield, J. F. Microbial Communities across a Hillslope-riparian Transect Shaped by Proximity to the Stream, Groundwater Table, and Weathered Bedrock. *Ecol. Evol.* **2019**, *9* (12), 6869−6900.
(70) Buchfink, B.; Reuter, K.; Drost, H.-G. Sensitive Protein Alignments at Tree-of-Life Scale Using DIAMOND. *Nat. Methods* **2021**, *18* (4), 366−368.
(71) Li, D.; Liu, C. M.; Luo, R.; Sadakane, K.; Lam, T. W. MEGAHIT: An Ultra-Fast Single-Node Solution for Large and Complex Metagenomics Assembly via Succinct de Bruijn Graph. *Bioinformatics* **2015**, *31* (10), 1674−1676.
(72) Chaumeil, P.-A.; Mussig, A. J.; Hugenholtz, P.; Parks, D. H. GTDB-Tk: A Toolkit to Classify Genomes with the Genome Taxonomy Database. *Bioinformatics* **2020**, *36*, 1925−1927.
(73) Shaffer, M.; Borton, M. A.; McGivern, B. B.; Zayed, A. A.; La Rosa, S. L.; Solden, L. M.; Liu, P.; Narrowe, A. B.; Rodríguez-Ramos, J.; Bolduc, B.; et al. DRAM for Distilling Microbial Metabolism to Automate the Curation of Microbiome Function. *Nucleic Acids Res.* **2020**, *48* (16), 8883−8900.

Downloaded from pubs.acs.org/esthag/article-pdf/60/32/22397/6456396/acs.est.6c03515.pdf by guest on 19 August 2026

https://doi.org/10.1021/acs.est.6c03515
Environ. Sci. Technol. 2026, 60, 22397−22407